Thickness-dependent topological phase transition and Rashba-like preformed topological surface states of α-Sn(001) thin films on InSb(001)

K. H. M. Chen [1,*] K. Y. Lin [2,*] S. W. Lien,[3] S. W. Huang,[1] C. K. Cheng [2] H. Y. Lin,[1] C.-H. Hsu,[4]
T.-R. Chang,[3,5,6,†] C.-M. Cheng [4,7,8,‡] M. Hong,[2,§] and J. Kwo [1,∥]

[1]*Department of Physics, National Tsing Hua University, Hsinchu 30013, Taiwan*
[2]*Graduate Institute of Applied Physics and Department of Physics, National Taiwan University, Taipei 10617, Taiwan*
[3]*Department of Physics, National Cheng Kung University, Tainan 70101, Taiwan*
[4]*National Synchrotron Radiation Research Center, Hsinchu 30076, Taiwan*
[5]*Center for Quantum Frontiers of Research and Technology (QFort), Tainan 70101, Taiwan*
[6]*Physics Division, National Center for Theoretical Sciences, National Taiwan University, Taipei 10617, Taiwan*
[7]*Department of Physics, National Sun Yat-sen University, Kaohsiung 80424, Taiwan*
[8]*Taiwan Consortium of Emergent Crystalline Materials, Ministry of Science and Technology, Taipei 10601, Taiwan*

Topological materials, possessing spin-momentum locked topological surface states (TSS), have attracted much interest due to their potential applications in spintronics. α-phase Sn (α-Sn), being one of them, displays enriched topological phases via band-gap engineering through a strain or confinement effect. In this work, we investigated the band evolution of in-plane compressively strained α-Sn(001) thin films on InSb(001) in a wide range of thickness from 3 bilayers (BL) to 370 BL by combining angle-resolved photoemission spectra and first-principles calculations. Gapped surface states evolved to a linearly dispersive TSS at a critical thickness of 6 BL, indicating that the system undergoes a phase transition from topologically trivial to nontrivial. For films thicker than 30 BL, additional Rashba-like surface states (RSS) were identified. These RSS served as preformed TSS in another strain-induced topological phase transition. In thick films, 370-BL α-Sn(001), so as to preclude the confinement effect in thin films, our results were consistent with a Dirac semimetal phase with Dirac nodes located along Γ–Z. This thickness-dependent band-structure study deepens our understanding of topological phase transitions and the evolution of Dirac states. Furthermore, the coexistence of TSS and RSS in a Dirac semimetal α-Sn might significantly enhance the potential for spintronic applications.

DOI: 10.1103/PhysRevB.105.075109

I. INTRODUCTION

The diverse topological phases of matter have been feverishly studied not only for scientific interest but also for their potential applications [1–6]. Featured by their special Dirac cones in the band structure, novel quantum oscillations are frequently observed in systems hosting Dirac fermions [7,8]. Extremely large linear magnetoresistance and a chiral magnetic effect have been found in Dirac and Weyl semimetals [7]. Applications utilizing these Dirac states are now being extensively investigated in many fields including thermoelectric devices, photonic devices, spin-based field-effect transistors and memories, etc. [5,6,9–11]. α-phase Sn (α-Sn), a group-IV element with a diamond structure, is one material that provides an ideal platform to realize abundant topological phases based on its nontrivial band topology. Unlike other group-IV elements such as Si and Ge, α-Sn is a zero-gap semiconductor with inverted p-like Γ_8 and s-like Γ_7^- bands [12,13],

which is similar to the band ordering of HgTe and some half-Heusler compounds [14,15]. In addition, α-Sn is free from off-stoichiometry and the related defect issues in compound materials through its elemental nature, making α-Sn promising for high-mobility Dirac fermion transport. Moreover, a large spin-to-charge conversion at room temperature and an efficient current-induced magnetization switching have been demonstrated in α-Sn/magnetic metal heterostructures, making α-Sn attractive for spintronic applications [16–18]. As a nontoxic group-IV member with inverted bands, α-Sn offers more advantages than other compound topological materials for the development of technology.

In the exploration of topological phase transitions, band-gap engineering via a quantum-confinement effect or strain modulation has been a commonly adopted route other than chemical doping [19,20]. Band evolution in a few atomic layers of thin films attracts much attention as the confinement effect has a significant influence on the band gap. A thickness-dependent topological phase transition typically occurs when the system endures a band inversion during the band-gap engineering. A single-layer α-Sn, especially in orientation (111), is of great interest because of its honeycomblike structure analogous to graphene and a large quantum spin Hall gap, 0.1–0.44 eV [21–23]. As the film becomes thicker, a two-dimensional (2D) to three-dimensional (3D) band transition

occurs; the unstrained α-Sn becomes a zero-gap semiconductor. With a further biaxial compressive (tensile) strain applied in plane, the system becomes a Dirac semimetal (topological insulator, TI) [24–26]. Besides the interesting phase transition found in α-Sn(111), band evolution in orientation (001) is worth studying and has yet to be fully explored in a wide range of thickness. Initiating from the reported topological surface states (TSS) connecting the inverted bulk bands in α-Sn(001) and α-Sn(111) [24,26–30], investigating how the TSS form and evolve in varied topological phases provides an insightful perspective on the phase transitions.

In this work, we have studied the electronic structure of in-plane compressively strained α-Sn(001) on InSb(001) substrates with thickness varied from a few bilayers (BL) to 370 BL. Comprehensive angle-resolved photoemission spectroscopy (ARPES) experiments were undertaken on high-quality α-Sn thin films prepared by molecular-beam epitaxy (MBE). Compared with previous work [27,28,31], our films exhibited excellent crystallinity and showed clear band dispersions with sharp TSS. A critical thickness, 6 BL, for the transition between topologically trivial and nontrivial phases was experimentally determined in undoped α-Sn(001) thin films. As the film thickness exceeded 30 BL, additional Rashba-like surface states (RSS) were identified and were associated with the preformed topological surface states in the phase transition to a 3D TI. Moreover, compared with calculations according to density-functional theory (DFT), 3D Dirac nodes were found at $k_z \sim 0.0276 \, \text{Å}^{-1}$ away from the Γ point around the Fermi energy (E_F). The thickness- and strain-dependent topological phase transitions in α-Sn(001) provide fruitful insight into the surface electronic structure of α-Sn and could be generalized to other Dirac materials.

II. METHODS

The preparation and characterization of α-Sn thin films on InSb(001) are described as follows. The InSb substrate treatment in this work is referred to the method in the literature [32,33]. The base pressure of the MBE chamber was less than 4×10^{-10} Torr. An InSb epilayer (thickness 235 nm) with growth rate 0.47 μm/h was deposited to ensure a smooth initial surface for the α-Sn growth (see Sec. I of the Supplemental Material [34]). The substrate temperature was then decreased below room temperature for deposition of Sn. Varied growth rates of α-Sn were adopted depending on the film thickness. Respectively, 160, 40, and 5.3 s/BL were used for few-, 30-, and 370-BL α-Sn(001) films. One BL of α-Sn(001) corresponds to a half conventional unit cell as shown in Fig. 1(a). Clear reflection high-energy electron diffraction (RHEED) intensity oscillations were observed during the growth of all films, indicating a layer-by-layer growth mode and providing a precise thickness control (Fig. S2(a) in Sec. II of the Supplemental Material [34]). The ARPES measurements were performed at beamline BL21B1 of Taiwan Light Source (TLS) in National Synchrotron Radiation Research Center (NSRRC). All data were recorded using an analyzer (Scienta R4000) with accepting angle $\pm 15°$. The overall energy resolution determined from the Fermi edge of a Au thin film was about 30 meV. X-ray diffraction (XRD) measurements were conducted at beamlines BL07A, BL13A,
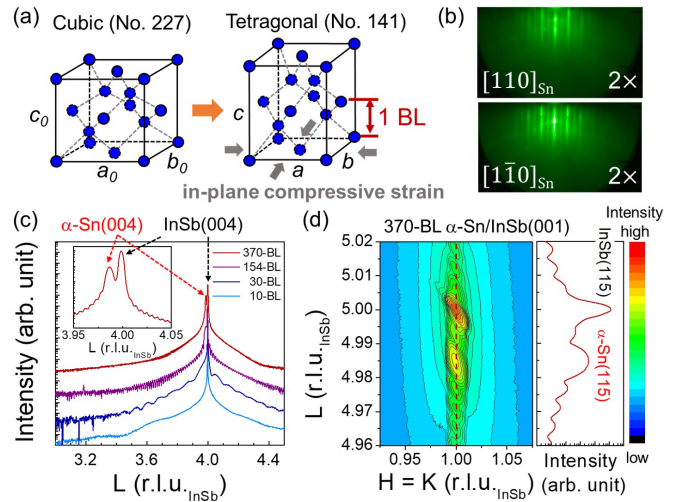

FIG. 1. (a) Crystal models of unstrained and strained α-Sn(001); the lattice parameters a_0, b_0, and c_0 in unstrained α-Sn(001) are 6.489 Å; the in-plane lattice parameters a and b of strained α-Sn/InSb(001) are 6.479 Å; the out-of-plane lattice parameter c of strained α-Sn/InSb(001) is 6.501 Å. (b) RHEED patterns of 30-BL α-Sn(001). (c) XRD radial scans across the α-Sn and InSb (004) reflections of samples with various thicknesses showing clear Pendellösung fringes. Inset: enlarged figure of 370-BL α-Sn/InSb(001) near (004) reflection. (d) Reciprocal-space map around the (115) reflections of α-Sn and InSb and the corresponding L scan across both reflections of 370-BL α-Sn/InSb(001).

and BL17B of TLS in NSRRC. Surface morphologies of α-Sn were characterized using an atomic-force microscope (AFM, with a Park XE-100 system).

Theoretical calculations of the α-Sn band structure were based on the projector augmented-wave method as implemented in the Vienna *Ab initio* Simulation Package (VASP) within the generalized gradient approximation scheme, with spin-orbit coupling (SOC) included. A Gamma-Pack k-point mesh $13 \times 13 \times 7$ was used; the lattice parameters were based on experimental values measured with XRD. The atomic positions were relaxed until the residual forces were less than 0.001 eV/Å. For the surface electronic structure, a slab model was used with the surface terminated by hydrogen to eliminate dangling bonds. The surface spectral weight was calculated using the semi-infinite Green's function approach [35] with an additional Rashba SOC considered.

III. RESULTS AND DISCUSSION

An unstrained α-Sn single crystal has a diamond structure with lattice parameter 6.489 Å. To date, most stable α-Sn films were pseudomorphically grown on semiconducting InSb or CdTe substrates. A slight in-plane compressive strain in α-Sn thin films naturally occurs because of the lattice mismatch ($\sim 0.15\%$) with the substrate, regardless of (001)- or (111)-oriented heterostructures. In α-Sn/InSb(001), the crystal symmetry of α-Sn changes from cubic (space group No. 227) to tetragonal (No. 141), as illustrated in Fig. 1(a). Strained α-Sn thin films were grown directly on well-prepared InSb(001) episurfaces with no intentional doping. The crystal structure of α-Sn was then characterized with RHEED,
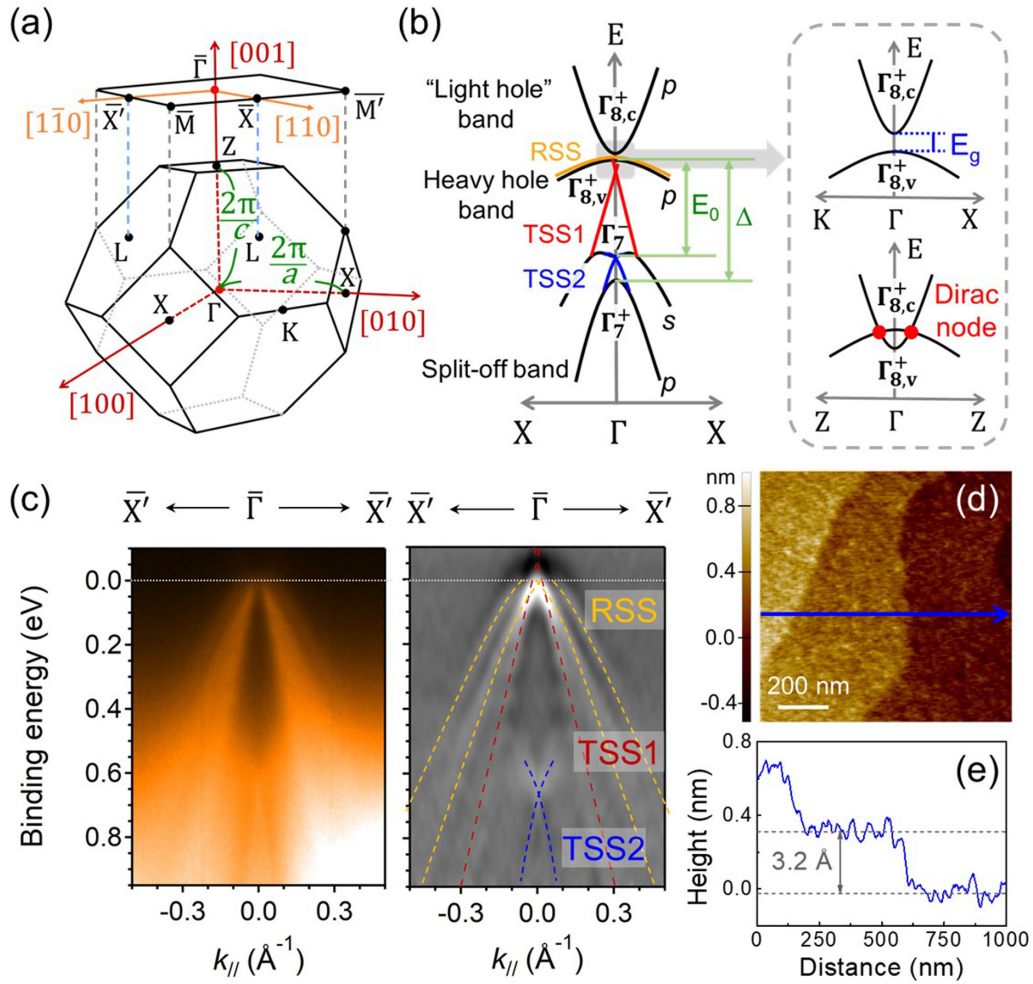
FIG. 2. (a) Bulk and surface BZ of strained α-Sn(001); (b) schematic band diagram of in-plane compressively strained α-Sn(001); (c) ARPES spectra and the second derivative plot of 30-BL α-Sn/InSb(001) taken with incident photon energy 21.2 eV along $\bar{\Gamma}$–$\bar{X'}$ at room temperature; (d) surface morphology; and (e) the line profile of the blue arrow in (d) of 30-BL α-Sn(001) by AFM.

low-energy electron diffraction (LEED), and XRD. The surface reconstruction (2 × 1) of α-Sn(001) was found in RHEED and LEED patterns (Fig. 1(b) and Fig. S2(b) in Sec. II of the Supplemental Material [34]), indicating a well-ordered surface. Excellent strained growth from a few BL to 370 BL was achieved and verified with XRD. Pronounced Pendellösung fringes were observed in the L scans across the (004) and (115) reflections as shown in Figs. 1(c) and 1(d), indicating sharp interfaces. The narrow rocking curve of the α-Sn(004) reflection, with a full width 0.0264° at half maximum (370-BL α-Sn) near that of the InSb(004), 0.0263°, revealed the excellent crystallinity and a low defect density. According to the XRD reciprocal-space map shown in Fig. 1(d), the lateral peak position of the α-Sn (115) reflection is well aligned with that of InSb, manifesting that a fully strained epitaxial α-Sn film on InSb(001) is retained even for the 370-BL (120-nm) film. Furthermore, the in-plane strain along two orthogonal directions [110] and [1$\bar{1}$0] were the same as verified in measurements of two off-normal reflections (115) and (1$\bar{1}$5), revealing a tetragonal lattice deformation and a biaxial in-plane compressive strain 0.15%. The measured in-plane and out-of-plane lattice parameters were 6.479 and 6.501 Å, respectively. More details of the strain analysis and

measurement of the lattice parameters appear in Sec. III of the Supplemental Material [34] (see also Refs. [36,37]).

After the crystal structure and strain state of α-Sn thin films were confirmed, the samples were ready for ARPES measurements of the thickness-dependent topological band structure. The bulk and surface Brillouin zones (BZ) of strained α-Sn(001) are shown in Fig. 2(a). Similar to the inverted band structure in HgTe, a heavy hole band ($\Gamma_{8,v}^+$) lies between inverted bands $\Gamma_{8,c}^+$ and Γ_7^- [15,38]. Γ_7^+ is below Γ_7^- because of the strong SOC; this effect generates a second band inversion in α-Sn [12,24]. The notation used in describing TSS in this work is referred to the previous study by Rogalev *et al.* [24]. TSS1 connects the inverted bands of $\Gamma_{8,c}^+$ and Γ_7^-, whereas TSS2 links the inverted bands of Γ_7^- and Γ_7^+ as shown in Fig. 2(b). The in-plane biaxial compressive strain in α-Sn grown on InSb breaks the cubic symmetry and introduces an energy gap at the Γ point. α-Sn enters the topological Dirac semimetal (TDS) phase with a pair of Dirac nodes located in Γ–Z. At a moderate thickness, 30 BL, of α-Sn(001), both TSS1 and TSS2 were clearly observed at room temperature [Fig. 2(c)]. Furthermore, large terraces with root-mean-square roughness 0.9 Å were achieved as shown in Fig. 2(d). The step height ∼3.2 Å corresponds to the
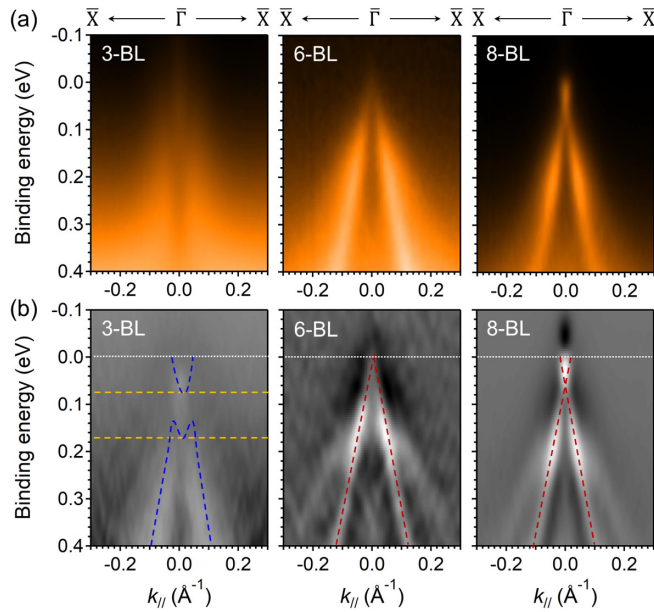
FIG. 3. (a) ARPES spectra of 3-, 6-, and 8-BL α-Sn(001) along $\bar{\Gamma}$–$\bar{X}$ with incident photon energy 21.2 eV; (b) second derivative plots of (a).

thickness of 1-BL α-Sn(001). The smooth and atomically flat surface is an important factor in yielding these sharp ARPES spectra.

Under effective control of substrate temperature and growth rate, the interdiffusion problem between film and substrate was greatly reduced (see Sec. IV of the Supplemental Material [34]). Our results indicate that the excellent crystallinity to detect the TSS was achieved without the commonly used Te dopants or Bi surface treatment in α-Sn growth [24,27,28]. The pure α-Sn films offer advantages for study of the band topology. Notably, distinct RSS bands appeared in the band-mapping results. The in-depth discussion of the RSS will be presented in later paragraphs. The band dispersions along $\bar{\Gamma}$–$\bar{X}$ and $\bar{\Gamma}$–$\bar{X'}$ are identical in 30-BL α-Sn, indicating the consistency with the fourfold rotational symmetry observed from RHEED and LEED patterns. The Fermi velocity of TSS1 is 5.2×10^5 m/s, which agrees with the value of pure α-Sn [$(4.8$–$5.2) \times 10^5$ m/s] [39]. Moreover, in contrast to the Dirac point (DP) located at 150 meV above E_F in previous work [31], a clear difference in this work is that the DP was located almost at E_F. The notable difference in the position of the DP between this work and other is attributed to less interdiffused indium atoms with improved methods of sample preparation. The higher chemical potential in our α-Sn films gave us access to study the evolution of TSS.

The band evolution in a few BL of α-Sn is discussed here, focusing on the evolution of TSS1. Before α-Sn growth, clear band mappings of bare InSb(001)-4 × 2/c(8 × 2) substrates are presented in Sec. I of the Supplemental Material [34] (see also Ref. [40] therein), indicating an atomically ordered surface. After the deposition of 3-BL α-Sn, α-Sn bands emerged clearly and behaved much different from that of InSb. Figure 3 displays ARPES spectra of these few BL (3-, 6-, and 8-BL) α-Sn samples and the corresponding second

derivative plots along $\bar{\Gamma}$–$\bar{X}$ measured with an incident photon energy 21.2 eV. An M-shaped hole band and a V-shaped electron pocket were found in the 3-BL sample, attributed to a wave-function hybridization of top and bottom surface states [41]. The conduction-band minimum was located at binding energy (E_B) ~ 0.07 eV and the valence-band maximum was at ~ 0.17 eV E_B at $\bar{\Gamma}$. The gap size was about 100 meV. Detailed analysis on the evolution of TSS1 from the normal emission spectra is given in Sec. V of the Supplemental Material [34]. The separated hole and electron bands transformed into a linearly dispersive TSS1 as the film became thicker than 6 BL. In an 8-BL sample, sharper ARPES spectra with a gapless TSS1 were attained. The TSS1 in the 8-BL sample had the same Fermi velocity as that in 6-BL and 30-BL ones. This experimental observation of a critical thickness in the topological phase transition is close to our DFT calculations (see Sec. VI of the Supplemental Material [34]) and a recent prediction in freestanding α-Sn(001) [41].

During the survey of TSS in α-Sn, we discovered an extra pair of surface states located outside TSS1 in all α-Sn films thicker than 30 BL. These extra surface states behaved as RSS manifested by a pair of paraboliclike bands with a momentum shift along $\bar{\Gamma}$–$\bar{X}$ and $\bar{\Gamma}$–$\bar{X'}$ as shown in Figs. 2(c) and 4(b). Figure 4(a) exhibits the constant energy mappings of 370-BL α-Sn; distinct squarelike intensity distributions (yellow arrows) were observed outside the Dirac cone of TSS1 (red dashed lines). Band mappings and DFT results along $\bar{\Gamma}$–$\bar{X}$ and $\bar{\Gamma}$–$\bar{M}$ are displayed in Figs. 4(b)–4(e). A significant difference of band structures in these two high-symmetry directions is that a large band splitting of RSS was clearly resolved in $\bar{\Gamma}$–$\bar{X}$, whereas the band splitting of RSS was minuscule in $\bar{\Gamma}$–$\bar{M}$, indicating an anisotropic behavior of the RSS. In our DFT calculations, spin-split surface bands, a typical characteristic of RSS, were observed. Note that to achieve an excellent agreement with the experimental results, an additional Rashba SOC was included in the DFT calculations; without this Rashba SOC, the RSS still existed but the band splitting in momentum was rather small (see Sec. VII of the Supplemental Material [34]). The surface potential of α-Sn was modified by a Rashba Hamiltonian H_R, $H_R = R \sum_{n,k_{\parallel}} c^{\dagger}_{n,k_{\parallel}} (\sigma_y \sin k_x a - \sigma_x \sin k_y a) c_{n,k_{\parallel}}$, in which R, n, σ_i, and a are the magnitude of the Rashba effect, the index of orbitals in the system, Pauli matrices, and the lattice parameter, respectively [42]. $R = 0.2$ eV was used here. The 2D characteristics of the RSS and TSS1 were examined with a measurement dependent on photon energy, as shown in Fig. 4(f). A dispersionless behavior in the plot of k_z versus $k_{\parallel}$ indicated the 2D nature for RSS and TSS1 bands. In the E–k cuts parallel to $\bar{\Gamma}$–$\bar{M}$ (cuts 1 and 3) shown in Figs. 4(g) and 4(h), a clear splitting of the RSS was observed, consistent with the two surface bands identified in $\bar{\Gamma}$–$\bar{X}$. The RSS were more dispersive in $\bar{\Gamma}$–$\bar{M}$ than in $\bar{\Gamma}$–$\bar{X}$. This anisotropic behavior of RSS is correlated to a warping effect caused by the crystal symmetry in α-Sn(001). In addition, a Rashba coefficient $\alpha_R \sim 1.5$ eVÅ was estimated from the band dispersion along $\bar{\Gamma}$–$\bar{X}$ (see Sec. VIII of the Supplemental Material [34]), and is $\sim 4.5\times$ larger than that of Au(111) [43].

Observing such a large Rashba band splitting is remarkable in the surface of a single-element crystal. In systems
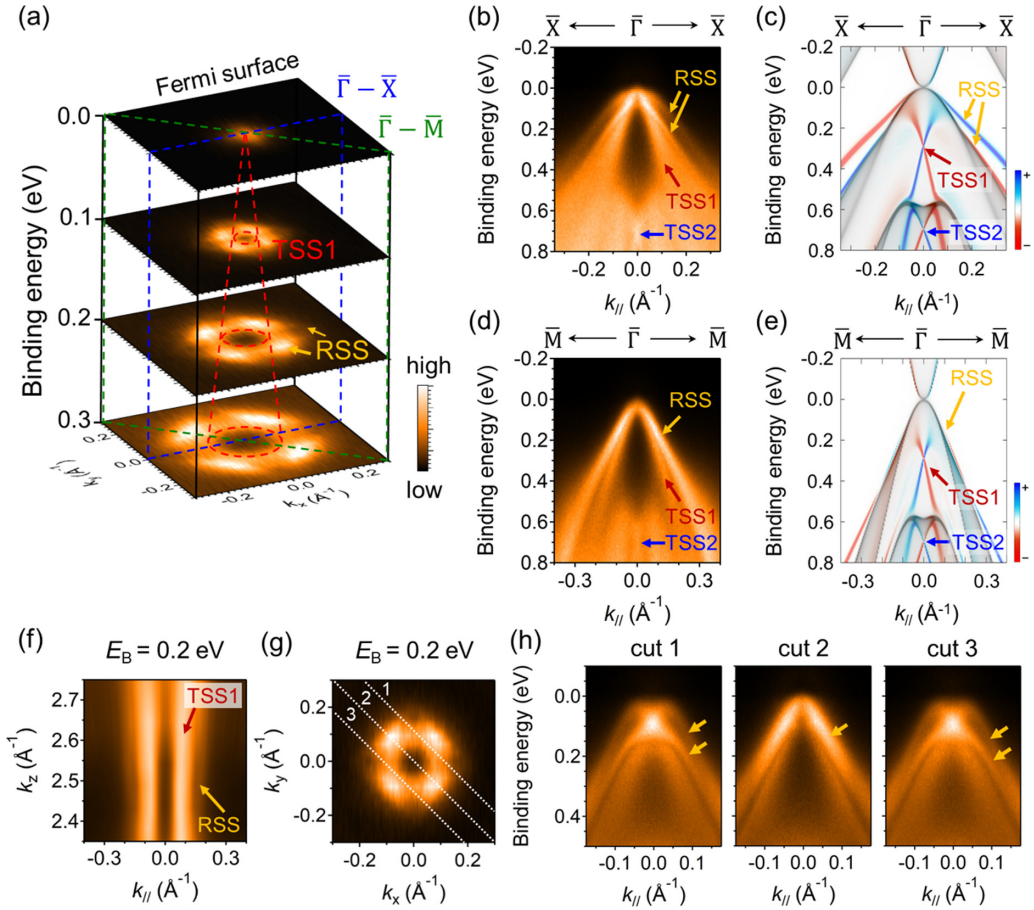
FIG. 4. (a) Stack of constant energy contours of 370-BL strained α-Sn(001) thin film with TSS1 marked in red dashed line and RSS marked with yellow arrows. (b) ARPES spectra and (c) DFT results along $\bar{\Gamma}$–$\bar{X}$; (d) ARPES spectra and (e) DFT results along $\bar{\Gamma}$–$\bar{M}$; the red and the blue curves in the DFT calculations are spin-polarized surface states with the spin projections along [1$\bar{1}$0] for band mapping along $\bar{\Gamma}$–$\bar{X}$ and along [010] for band mapping along $\bar{\Gamma}$–$\bar{M}$; the colors denote the spin polarization as shown in the color scale; the gray bands are bulk bands. (f) k_z–$k_{//}$ plot ($k_{//}$ along $\bar{\Gamma}$–$\bar{X}$) at 0.2 eV E_B; (g) constant energy contour at 0.2 eV E_B; (h) ARPES spectra along $\bar{\Gamma}$–$\bar{M}$ (cut 2) and other parallel cuts (1 and 3); each cut is separated by 0.078 Å^{-1} with its direction labeled in (g); all ARPES spectra were acquired with incident photon energy 20 eV.

possessing a large Rashba effect, besides a strong SOC, inversion asymmetry is essential. As the bulk inversion symmetry is still preserved for in-plane biaxially strained α-Sn(001) films, the RSS are related to the structural inversion asymmetry on the surface. Instead of finding these RSS in extremely thin films, in which a quantum-confinement effect and a substrate effect play major roles, the observed RSS in thick α-Sn films indicated their origin to be merely from the upper surface. We noticed also that the orientation for the largest band splitting, $\bar{\Gamma}$–$\bar{X}$ or $\bar{\Gamma}$–$\bar{X'}$, is parallel to the dimer rows on the (2×1)-reconstructed α-Sn surfaces; the surface potential of the dimered surface could hence be a reason for this large band splitting. The surface Sn dimers could act as dipoles [44], providing a necessary electric field to account for the Rashba band splitting.

Inspired by the band evolution of TSS in a topological phase transition from a normal insulator to a 3D TI [42,45], the appearance of the RSS in a Dirac semimetal strained α-Sn(001) can be regarded as the preformed surface states of another TSS. As illustrated in Fig. 5(a), the RSS of a normal insulator in bulk conduction bands (BCB) and bulk valence bands (BVB) touch each other and form a gapless state as the

band inversion occurs. One pair of preformed surface states in the BCB and the BVB evolves to a TSS; the other pair becomes surface resonance states and damps into bulk bands. Dirac semimetals could serve as one topological phase at the critical point of the topological phase transition, but RSS have not yet been found in previously reported Dirac semimetals. Having substantially good surfaces of Dirac semimetals for ARPES measurements is also challenging, especially for thin films. In this work, elemental Dirac semimetal α-Sn(001) thin films with far fewer defects can be viewed as an ideal intermediate state among the transitions to trivial insulating and many other topological phases, providing an excellent platform to study the TSS evolution. For instance, α-Sn can turn into a 3D TI with an applied in-plane biaxial tensile strain or in-plane uniaxial strain. According to our DFT results, the original TDS of an in-plane biaxial compressive strained α-Sn [Fig. 5(b)] becomes a 3D TI featuring a TSS formed in the bulk band gap under an applied in-plane uniaxial strain [Fig. 5(c)]. Investigation of RSS in a topological system not limited to TI but also for other semimetals provides profound insight into the origin of TSS. For TSS in Dirac semimetals, most studies focused on Fermi arcs connecting the Dirac
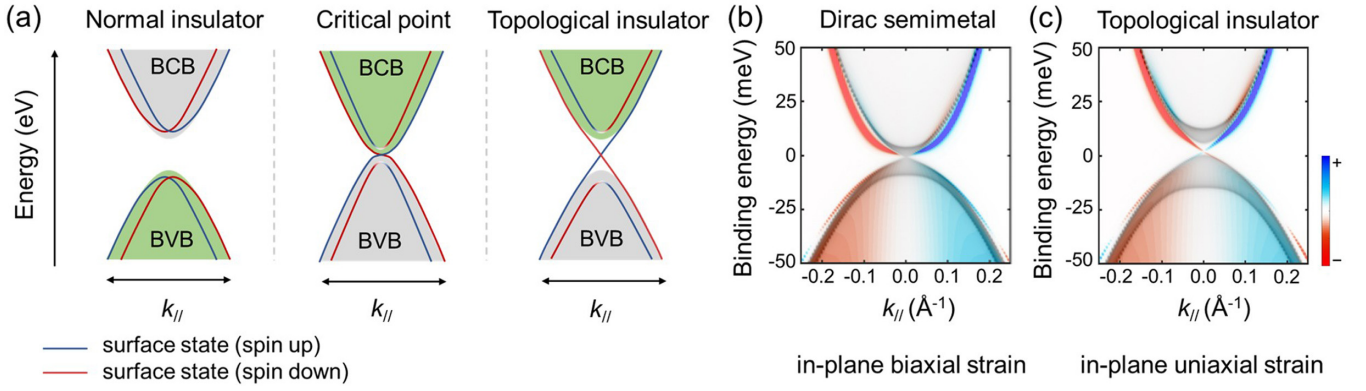
FIG. 5. (a) Schematic of the band evolution of the RSS and TSS in a topological phase transition; DFT results of α-Sn(001) along $\bar{\Gamma}-\bar{M}$ under (b) an in-plane biaxial compressive strain 0.15% and (c) an in-plane uniaxial compressive strain 0.6% with no additional Rashba SOC. The red and the blue curves in the DFT calculations are spin-polarized surface states with the spin projections along [010]; the colors denotes the spin polarization as shown in the color scale and the gray bands are bulk bands.

nodes. Our work indicates that the RSS in (001) are other surface states, besides the Fermi arcs predicted in (100) [25], correlated with the band topology in the Dirac semimetal of strained α-Sn. Having RSS coexisting with TSS1 could provide an efficient and gate-tunable spin-charge conversion [46,47], which offers great potential in spintronics.

In the following, we focus on the behavior of the bulk bands in search of 3D Dirac bands or nodes in α-Sn(001), which has previously not been demonstrated experimentally. The ARPES results of α-Sn were nearly the same for films thicker than 30 BL. To preclude the confinement effect commonly found in few-BL films, a thicker film, 370 BL, of

α-Sn was prepared to probe the bulk band structure. The momenta k_z along $\Gamma-Z$ were determined from a photon energy-dependent experiment with an inner potential V_0 9.3 $\pm$ 0.5 eV (see Sec. IX of the Supplemental Material [34]). Figure 6(a) shows clear bulk bands instead of quantized subbands in the band mapping measured along [100] ($\bar{\Gamma}-\bar{M}$) using photon energy 123.5 eV (Γ_{003}) at 80 K. Calculated bands along [100] [Fig. 6(b)] were overlaid on the band mapping with green dots in Fig. 6(a), revealing a considerably good match with each other. Clear bulk bands of $\Gamma_{8,v}^+$, Γ_7^-, and Γ_7^+ at the Γ point were also identified. The energy separation E_0 between p-like $\Gamma_{8,v}^+$ and s-like Γ_7^- is 0.60 eV and the split-off energy Δ
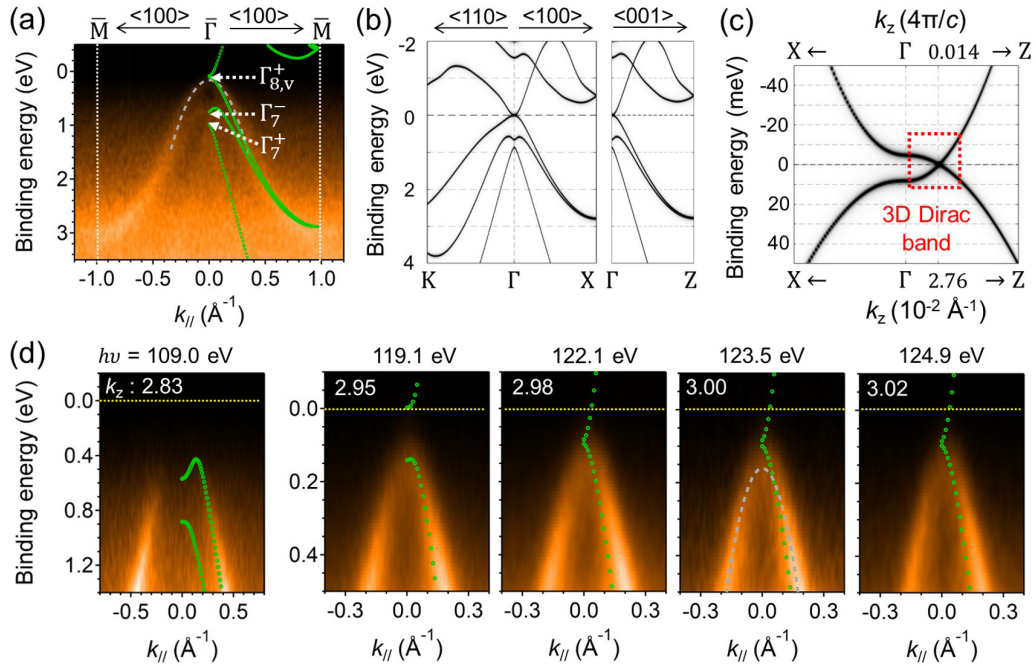

FIG. 6. (a) ARPES results of 370-BL α-Sn(001) at Γ_{003}; (b) DFT-calculated band structure of α-Sn(001) under in-plane biaxial compressive strain 0.15%; (c) magnified figure in the vicinity of Γ in $X-\Gamma-Z$; (d) photon energy-dependent ARPES results of $\Gamma_{8,v}^+$ near Γ_{003} along $\bar{\Gamma}-\bar{M}$ with their corresponding k_z values at E_F in unit $4\pi/c$. The gray dashed line and green dots superimposed in (a) and (d) are parabolic fitting of the heavy hole band and DFT calculations, respectively.

between $\Gamma_{8,v}^+$ and Γ_7^+ is 0.84 eV in the presence of SOC; these directly measured results are consistent with our DFT calculations and earlier work using other techniques [12,48,49]. Considering a nearly free-electron model for the heavy hole band at the Γ point, a fitted parabolic band dispersion was superimposed on the band mapping with a gray dashed line. The effective mass was derived to be $0.34 \pm 0.05\, m_0$ along [100], in which m_0 is the electron rest mass, slightly larger than the unstrained one ($0.26\, m_0$) obtained from band calculations [50,51]. Benefiting from greatly reduced interdiffusion from the substrate–film interface, $\Gamma_{8,v}^+$ was observed at ~ 0.16 eV E_B; this result provided an opportunity to search for Dirac nodes in in-plane compressively strained α-Sn(001).

According to the DFT calculations in Figs. 6(b) and 6(c), the predicted Dirac nodes were located at ±0.0276 Å^{-1} ($\pm 0.014 \cdot 4\pi/c$) away from the Γ point in Γ–Z. The linearly dispersive Dirac bands were limited to a small E–k region marked as a red box in Fig. 6(c). A small energy gap of 17 meV appeared at the zone center because of the cubic symmetry breaking in the in-plane compressively strained α-Sn(001). The photon energy-dependent ARPES spectra of the heavy hole band near Γ_{003} and E_F agreed well with the DFT results, as shown in Fig. 6(d). The Dirac nodes were located approximately at the spectra taken at 122.1 and 124.9 eV. Along Γ–Z, the 3D Dirac band in strained α-Sn(001) was less dispersive than that reported for strained α-Sn(111) within $\pm5\%$ of the band periodicity [26]. The calculated separation of the 3D Dirac nodes in α-Sn/InSb(001) (~0.06 Å^{-1}) caused by the in-plane compressive strain (0.15%) was 1/3 to 1/5 those of other Dirac semimetals such as Na$_3$Bi (0.19 Å^{-1}) [52] and Cd$_3$As$_2$ (0.32 Å^{-1}) [53]. Hence, resolving the two separate 3D Dirac nodes and linearly dispersive Dirac bands unambiguously is much more difficult in strained α-Sn(001)/InSb.

IV. CONCLUSION

We report here a comprehensive study of the electronic structure of compressively strained α-Sn/InSb(001). Considerably purer α-Sn films were prepared with MBE, leading to sharp ARPES spectra for a thorough understanding of the topological band structure. A transition from a topologically trivial to nontrivial phase was observed at critical thickness 6 BL. A pair of anisotropic RSS were discovered in α-Sn(001)

films thicker than 30 BL; they were regarded as preformed TSS, providing insight into the evolution of a TSS in a topological phase transition and the surface electronic structure of a Dirac material. In a 370-BL film, which is thick enough to preclude the confinement effect, both the bulk band dispersions and the valence-band parameters have been directly measured. Supported by the DFT results, the Dirac nodes were found in our strained α-Sn/InSb(001) but were difficult to resolve individually in ARPES spectra because of the small momentum separation in Γ–Z. A more viable approach would be to adopt another substrate with a smaller lattice parameter to produce a greater in-plane biaxial compressive strain in α-Sn for a wider separation of Dirac nodes in k space. As revealed by our results, α-Sn provides a rich playground to realize various topological phases of matter, such as TDS, TI, etc. The coexistence of RSS and TSS1, typified by an efficient and gate-tunable spin-charge conversion, might offer great opportunities for applications in the modern technology of spintronics.

[1] M. Z. Hasan and C. L. Kane, Rev. Mod. Phys. **82**, 3045 (2010).

[2] L. Fu and C. L. Kane, Phys. Rev. B **76**, 045302 (2007).

[3] N. P. Armitage, E. J. Mele, and A. Vishwanath, Rev. Mod. Phys. **90**, 015001 (2018).

[4] Z. Wang, Y. Sun, X.-Q. Chen, C. Franchini, G. Xu, H. Weng, X. Dai, and Z. Fang, Phys. Rev. B **85**, 195320 (2012).

[5] J. L. Collins, A. Tadich, W. Wu, L. C. Gomes, J. N. B. Rodrigues, C. Liu, J. Hellerstedt, H. Ryu, S. Tang, S.-K. Mo, S. Adam, S. A. Yang, M. S. Fuhrer, and M. T. Edmonds, Nature (London) **564**, 390 (2018).

[6] M. M. H. Polash, S. Yalameha, H. Zhou, K. Ahadi, Z. Nourbakhsh, and D. Vashaee, Mater. Sci. Eng. R Rep. **145**, 100620 (2021).

[7] J. Hu, S.-Y. Xu, N. Ni, and Z. Mao, Annu. Rev. Mater. Res. **49**, 207 (2019).

[8] Y. Ando, J. Phys. Soc. Jpn. **82**, 102001 (2013).

[9] A.-Q. Wang, X.-G. Ye, D.-P. Yu, and Z.-M. Liao, ACS Nano **14**, 3755 (2020).

[10] Y. Wu, C. Li, X. Hu, Y. Ao, Y. Zhao, and Q. Gong, Adv. Opt. Mater. **5**, 1700357 (2017).

[11] D. Pesin and A. H. MacDonald, Nat. Mater. **11**, 409 (2012).

[12] S. Küfner, J. Furthmüller, L. Matthes, M. Fitzner, and F. Bechstedt, Phys. Rev. B **87**, 235307 (2013).

[13] I. Pelant and K. Kůsová, Crystals **9**, 624 (2019).

[14] F. Casper, T. Graf, S. Chadov, B. Balke, and C. Felser, Semicond. Sci. Technol. **27**, 063001 (2012).

[15] J. Chu and A. Sher, *Physics and Properties of Narrow Gap Semiconductors* (Springer, New York, 2008).

[16] J.-C. Rojas-Sánchez, S. Oyarzún, Y. Fu, A. Marty, C. Vergnaud, S. Gambarelli, L. Vila, M. Jamet, Y. Ohtsubo, A. Taleb-Ibrahimi, P. Le Fèvre, F. Bertran, N. Reyren, J.-M. George, and A. Fert, Phys. Rev. Lett. **116**, 096602 (2016).

[17] J. Ding, C. Liu, Y. Zhang, V. Kalappattil, R. Yu, U. Erugu, J. Tang, H. Ding, H. Chen, and M. Wu, Adv. Funct. Mater. **31**, 2008411 (2021).

[18] J. Ding, C. Liu, V. Kalappattil, Y. Zhang, O. Mosendz, U. Erugu, R. Yu, J. Tian, A. DeMann, S. B. Field, X. Yang, H. Ding, J. Tang, B. Terris, A. Fert, H. Chen, and M. Wu, Adv. Mater. **33**, 2005909 (2021).

[19] Y. Zhang, K. He, C.-Z. Chang, C.-L. Song, L.-L. Wang, X. Chen, J.-F. Jia, Z. Fang, X. Dai, W.-Y. Shan, S.-Q. Shen, Q. Niu, X.-L. Qi, S.-C. Zhang, X.-C. Ma, and Q.-K. Xue, Nat. Phys. **6**, 584 (2010).

[20] J. Mutch, W.-C. Chen, P. Went, T. Qian, I. Z. Wilson, A. Andreev, C.-C. Chen, and J.-H. Chu, Sci. Adv. **5**, eaav9771 (2019).

[21] Y. Xu, B. Yan, H.-J. Zhang, J. Wang, G. Xu, P. Tang, W. Duan, and S.-C. Zhang, Phys. Rev. Lett. **111**, 136804 (2013).

[22] C.-Z. Xu, Y.-H. Chan, P. Chen, X. Wang, D. Flötotto, J. A. Hlevyack, G. Bian, S.-K. Mo, M.-Y. Chou, and T.-C. Chiang, Phys. Rev. B **97**, 035122 (2018).

[23] J. Deng, B. Xia, X. Ma, H. Chen, H. Shan, X. Zhai, B. Li, A. Zhao, Y. Xu, W. Duan, S.-C. Zhang, B. Wang, and J. G. Hou, Nat. Mater. **17**, 1081 (2018).

[24] V. A. Rogalev, T. Rauch, M. R. Scholz, F. Reis, L. Dudy, A. Fleszar, M.-A. Husanu, V. N. Strocov, J. Henk, I. Mertig, J. Schäfer, and R. Claessen, Phys. Rev. B **95**, 161117(R) (2017).

[25] H. Huang and F. Liu, Phys. Rev. B **95**, 201101(R) (2017).

[26] C.-Z. Xu, Y.-H. Chan, Y. Chen, P. Chen, X. Wang, C. Dejoie, M.-H. Wong, J. A. Hlevyack, H. Ryu, H.-Y. Kee, N. Tamura, M.-Y. Chou, Z. Hussain, S.-K. Mo, and T.-C. Chiang, Phys. Rev. Lett. **118**, 146402 (2017).

[27] A. Barfuss, L. Dudy, M. R. Scholz, H. Roth, P. Höpfner, C. Blumenstein, G. Landolt, J. H. Dil, N. C. Plumb, M. Radovic, A. Bostwick, E. Rotenberg, A. Fleszar, G. Bihlmayer, D. Wortmann, G. Li, W. Hanke, R. Claessen, and J. Schäfer, Phys. Rev. Lett. **111**, 157205 (2013).

[28] Y. Ohtsubo, P. Le Fèvre, F. Bertran, and A. Taleb-Ibrahimi, Phys. Rev. Lett. **111**, 216401 (2013).

[29] Z. Shi, X. Wang, C. Xu, P. Wang, Y. Liu, and T.-C. Chiang, Phys. Lett. A **384**, 126782 (2020).

[30] V. A. Rogalev, F. Reis, F. Adler, M. Bauernfeind, J. Erhardt, A. Kowalewski, M. R. Scholz, L. Dudy, L. B. Duffy, T. Hesjedal, M. Hoesch, G. Bihlmayer, J. Schäfer, and R. Claessen, Phys. Rev. B **100**, 245144 (2019).

[31] M. R. Scholz, V. A. Rogalev, L. Dudy, F. Reis, F. Adler, J. Aulbach, L. J. Collins-McIntyre, L. B. Duffy, H. F. Yang, Y. L. Chen, T. Hesjedal, Z. K. Liu, M. Hoesch, S. Muff, J. H. Dil, J. Schäfer, and R. Claessen, Phys. Rev. B **97**, 075101 (2018).

[32] W. K. Liu, W. T. Yuen, and R. A. Stradling, J. Vac. Sci. Technol. B **13**, 1539 (1995).

[33] W. K. Liu and M. B. Santos, J. Vac. Sci. Technol. B **14**, 647 (1996).

[34] See Supplemental Material at http://link.aps.org/supplemental/10.1103/PhysRevB.105.075109 for more material characterizations of α-Sn(001) and InSb(001), details of DFT calculations, estimate of the Rashba coefficient of RSS, and extra band-dispersions data along Γ–Z.

[35] G. W. Bryant, Phys. Rev. B **31**, 5166 (1985).

[36] J. Hornstra and W. J. Bartels, J. Cryst. Growth **44**, 513 (1978).

[37] S. Adachi, *Properties of Group-IV, III-V and II-VI Semiconductors* (John Wiley & Sons, Ltd., Chichester, 2005).

[38] C. H. L. Goodman, IEE Proceedings I (Solid-State and Electron Devices) **129**, 189 (1982).

[39] I. Madarevic, U. Thupakula, G. Lippertz, N. Claessens, P.-C. Lin, H. Bana, S. Gonzalez, G. Di Santo, L. Petaccia, M. N. Nair, L. M. C. Pereira, C. Van Haesendonck, and M. J. Van Bael, APL Mater. **8**, 031114 (2020).

[40] L. Walczak, G. Goryl, M. A. Valbuena, I. Vobornik, A. Tejeda, A. Taleb-Ibrahimi, J. J. Kolodziej, P. Segovia, and E. G. Michel, Surf. Sci. **608**, 22 (2013).

[41] J. Li and Y. Xu, Spin **9**, 1940012 (2019).

[42] C. Jozwiak, J. A. Sobota, K. Gotlieb, A. F. Kemper, C. R. Rotundu, R. J. Birgeneau, Z. Hussain, D.-H. Lee, Z.-X. Shen, and A. Lanzara, Nat. Commun. **7**, 13143 (2016).

[43] H. Cercellier, C. Didiot, Y. Fagot-Revurat, B. Kierren, L. Moreau, D. Malterre, and F. Reinert, Phys. Rev. B **73**, 195413 (2006).

[44] Z.-Y. Lu, G. L. Chiarotti, S. Scandolo, and E. Tosatti, Phys. Rev. B **58**, 13698 (1998).

[45] S.-Y. Xu, M. Neupane, I. Belopolski, C. Liu, N. Alidoust, G. Bian, S. Jia, G. Landolt, B. Slomski, J. H. Dil, P. P. Shibayev, S. Basak, T.-R. Chang, H.-T. Jeng, R. J. Cava, H. Lin, A. Bansil, and M. Z. Hasan, Nat. Commun. **6**, 6870 (2015).

[46] S. Shi, A. Wang, Y. Wang, R. Ramaswamy, L. Shen, J. Moon, D. Zhu, J. Yu, S. Oh, Y. Feng, and H. Yang, Phys. Rev. B **97**, 041115(R) (2018).

[47] R. Sun, S. Yang, X. Yang, E. Vetter, D. Sun, N. Li, L. Su, Y. Li, Y. Li, Z.-Z. Gong, Z.-K. Xie, K.-Y. Hou, Q. Gul, W. He, X.-Q. Zhang, and Z.-H. Cheng, Nano Lett. **19**, 4420 (2019).

[48] B. L. Booth and A. W. Ewald, Phys. Rev. **168**, 796 (1968).

[49] R. A. Carrasco, C. M. Zamarripa, S. Zollner, J. Menéndez, S. A. Chastang, J. Duan, G. J. Grzybowski, B. B. Claflin, and A. M. Kiefer, Appl. Phys. Lett. **113**, 232104 (2018).

[50] L. Liu and W. Leung, Phys. Rev. B **12**, 2336 (1975).

[51] D. Zhang, H. Wang, J. Ruan, G. Yao, and H. Zhang, Phys. Rev. B **97**, 195139 (2018).

[52] Z. K. Liu, B. Zhou, Y. Zhang, Z. J. Wang, H. M. Weng, D. Prabhakaran, S.-K. Mo, Z. X. Shen, Z. Fang, X. Dai, Z. Hussain, and Y. L. Chen, Science **343**, 864 (2014).

[53] Z. K. Liu, J. Jiang, B. Zhou, Z. J. Wang, Y. Zhang, H. M. Weng, D. Prabhakaran, S.-K. Mo, H. Peng, P. Dudin, T. Kim, M. Hoesch, Z. Fang, X. Dai, Z. X. Shen, D. L. Feng, Z. Hussain, and Y. L. Chen, Nat. Mater. **13**, 677 (2014).